Coarse-Grained Force Field Calibration Based on Multi-Objective Bayesian Optimization to Simulate Water Diffusion in Poly-ε-caprolactone

Jesse M. Sestito, Mary Thatcher, Leshi Shu, Tequila A.L. Harris, Yan Wang*

George W. Woodruff School of Mechanical Engineering, Georgia Institute of Technology,

801 Ferst Drive NW, Atlanta, GA 30332-0405, USA

Abstract

Molecular dynamics at the atomistic scale is increasingly being used to predict material properties and speed up the materials design and development process. However, the accuracy of molecular dynamics predictions is sensitively dependent on the force fields. In the traditional force field calibration process, a specific property, predicted by the model, is compared with the experimental observation and the force field parameters are adjusted to minimize the difference. This leads to the issue that the calibrated force fields are not generic and robust enough to predict different properties. Here, a new calibration method based on multi-objective Bayesian optimization is developed to speed up the development of molecular dynamics force fields that are capable of predicting multiple properties accurately. This is achieved by reducing the number of simulation runs to generate the Pareto front with an efficient sequential sampling strategy. The methodology is demonstrated by generating a new coarse-grained force field for polycaprolactone, where the force field can predict mechanical properties and water diffusion in the polymer.

Introduction

Molecular dynamics (MD) simulations predict the physical properties of materials by examining the movements of atomic particles as a result of the forces acting upon them. To simulate these forces, MD utilizes different types of force field models, mostly empirical. Many force fields are generated for specific materials to capture the interactions between the predefined types of atoms. For instance, the embedded atom method (EAM) potential for nickel only captures the nickel-nickel interactions,[1] and the modified embedded atom method (MEAM) potential for Nitinol only captures nickel and titanium interactions.[2] Usually a force field is calibrated by comparing one predicted property with the corresponding experimental observation and the model parameters are adjusted to minimize the difference. There are also more generic full-atom force fields that model different atom types such as the Dreiding force field for generic use cases.[3] These generic force fields have been further developed for material-specific simulations, such as Optimized Potential for Liquid Simulations (OPLS),[4,5] GROningen MOlecular Simulation program package (GROMOS) for biomolecular systems,[6] Chemistry at HARvard Macromolecular Mechanics (CHARMM) for biomolecules,[7] and Assisted Model Building and Energy Refinement (AMBER) for proteins, nucleic acids, and carbohydrates.[8] These force fields are useful for modeling general physical interactions of molecules. Similarly applying such force fields to specific material property calculations may yield inaccurate results if they are calibrated based on a different type of property. There is a great need for improved and robust force field models that are capable of predicting different properties simultaneously and accurately.

Several methods have been used to generate and calibrate force fields for specific use cases. Typically the calibration methods rely on experimental values of energy to parameterize the force field.[9,10]

This can be cumbersome due to experimental limitations and expenses. Quantum mechanics calculations such as density functional theory (DFT) have also been used in developing force fields.[11] DFT models also need to be calibrated and the associated errors can be propagated to force fields. In general, the calibration of force fields is an optimization process, where the parameters of the force fields are tuned to minimize the difference between the predicted property from the MD simulation and the reference value.[12] When multiple properties need to be considered simultaneously, this process becomes the multi-objective optimization. Very limited work has been done for multi-objective force field calibration. Ragasa et al. used a multi-objective optimization approach to develop a force field for magnesium oxide (MgO), where thousands of simulations were run first and a Gaussian model was then applied to select the best force fields to generate the Pareto front.[13] For computationally expensive MD simulations, more efficient sampling methods for optimization are needed. In this research, a multi-objective Bayesian optimization approach is proposed to counter this computational challenge. A sequential sampling strategy is taken in Bayesian optimization, where a surrogate model is constructed to approximate each objective function. In parallel an acquisition function is also constructed and used to decide the sample of parameter values to run the next simulation. The surrogates and the acquisition function are updated in each iteration of search. Compared to traditional sampling, Bayesian optimization methods can significantly reduce the required number of simulations. Single-objective Bayesian optimization was recently applied to parameterize force fields for dissipative particle dynamics.[14] General Bayesian reasoning[15,16] has also been used to parameterize force fields. The potential of multi-objective Bayesian optimization for force field parameterization however has not been explored. The multi-objective Bayesian optimization approaches can efficiently identify Pareto solutions[17,18] and help improve the robustness and versatility of parameterization for predicting multiple properties simultaneously.

Herein, the multi-objective Bayesian optimization is utilized to calibrate model parameters for multiple properties. We demonstrate this method by generating a coarse-grained force field of polycaprolactone (PCL) that is capable of predicting both the modulus of elasticity of the polymer matrix and the water diffusivity in the matrix. In order to simulate the tensile test and the diffusion of water through PCL effectively using MD, it is important to use a force field model parameterized accurately for both processes. Traditional MD with full atomistic force fields can only simulate very fast processes at the time scale of nanoseconds with a femtosecond time step. Full atomistic MD is computationally expensive for polymer solids due to the number of atoms and bonds, as well as angular and dihedral interactions. For example, an 80 kDa molecular weight chain of PCL contains 12,618 atoms per chain. Coupling this with 9 chains and simulating the diffusion process in the nanosecond range results in over 1.5×10^{20} physical interactions in one nanosecond. To counter these length- and time-scale challenges, a coarse-grained (CG) approach is taken to improve the simulation efficiency by reducing the number of particles per chain and increasing the time step.

CG force fields offer an alternative to MD simulations of full atomistic, united atom, and finitely extensible nonlinear elastic (FENE) models. CG force fields generally remove all the hydrogen and capture several large atoms as one particle. One such force field, the MARTINI force field, is a generic CG model geared for polymer and biomolecular simulations.[19] Not only can this model reduce the number of particles, but it also allows for a time step increase up to 40 femtoseconds. This force field provides the non-bonded particle interactions. But it must be calibrated through changing bond, angle, and dihedral interactions. Calibration has been done for several materials including water,[20] proteins,[21,22] polystyrene,[23]

polyethylene, and polytetrafluoroethylene.[24] Calibrations were done based on material properties such as the elastic modulus,[25] glass transition temperature,[26] heat capacity,[26] temperature transferability,[23] and viscosity.[27] MARTINI has also been used to analyze systems such as the stability of sodium dodecyl sulfate films with oil[28] and in aqueous solutions,[27] to simulate the sintering process of oxide fuel cells,[29] and to predict adhesion mechanics[30] and structure-property relationships.[31] Here, a MARTINI CG force field for PCL will be used to illustrate the new calibration process.

Methods

In traditional force field calibration, the optimization procedure is taken to minimize the difference between one predicted property from simulation and an experimental measurement. In the proposed approach, multiple properties are considered simultaneously, and a more efficient sequential sampling based multi-objective Bayesian optimization approach is introduced.

The force field calibration process in our approach consists of two stages, as outlined in Figure 1. First, the multi-objective optimization is formulated based on the properties of interest for a given application. MD models are set up. After some initial simulations to build the initial surrogate models, additional executions of MD are guided by sequential sampling. The optima or Pareto solutions are identified. Second, statistical analyses and validation are performed within the Pareto solutions. The solution set is narrowed down to a final force field recommendation with the considerations of uncertainty and robustness.

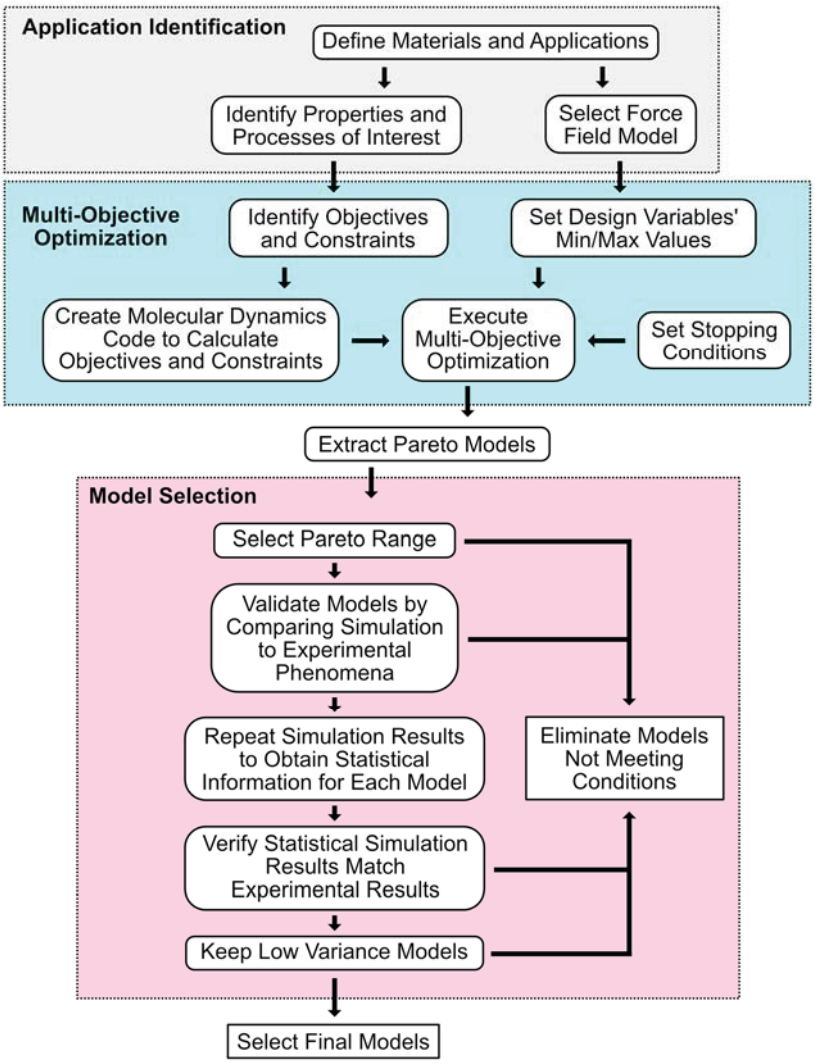

Figure 1. The proposed calibration process to generate molecular dynamics force fields based on multi-objective optimization.

In multi-objective optimization, there are conflicts between the multiple objectives. That is, choosing the optimal solution for one objective requires the compromise of others. For instance, when the minimization of two objectives is sought, as illustrated in Figure 2, it is not possible to find a solution such that both objectives are minimized. There is a subset of solutions on the Pareto front, or Pareto solutions, where improving one objective always requires the sacrifice of the other. The Pareto solutions are non-dominated solutions such that it is impossible to improve one objective without negatively impacting the other. Non-dominated solutions on the Pareto front are better than or dominate the ones in the other region. Seeking these Pareto solutions is the main goal of multi-objective optimization.

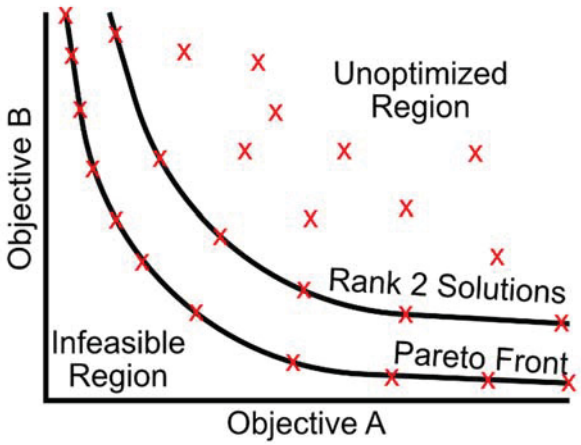

Figure 2. Illustration of the different regions in a multi-objective optimization problem.

Sampling efficiency is important for obtaining the Pareto solutions, especially for the computationally expensive MD simulations. The number of samples drawn that belong to dominated solutions need to be minimized. Here, we use a multi-objective Bayesian optimization approach to search for Pareto solutions. Bayesian optimization algorithms search optima on the surrogate models of the objective functions, where a sequential sampling strategy is taken based on some utility or acquisition functions. For each iteration, a new sample location is selected so that the acquisition function is maximized, and the surrogates are updated with the inclusion of the additional sample point. This sequential sampling procedure is the key to reduce the total computational time by predicting the next representative sample of parameters for the multi-objective optimization. It provides an efficient method for obtaining the Pareto solutions and selecting the optimal force field model.

Selecting an acquisition function to guide the sequential sampling in multi-objective Bayesian optimization to find the Pareto solutions is important. Here we use the expected improvement matrix (EIM) as the acquisition function that was proposed by Zhan et. al,[18] where each element in the EIM is the expected improvement for each sample point with respect to each objective**,** and an aggregated scalar value based on all elements in the EIM is used to guide the sampling. Note that the traditional expected improvement acquisition function[32] only supports single-objective optimization. Therefore such new definitions of acquisition functions are needed for multi-objective Bayesian optimization.

In our implementation, Gaussian process models are used as the surrogates of objective functions. Each Gaussian process surrogate is built with a zero-order polynomial regression model and a Gaussian correlation kernel. The implementation was based on the Design and Analysis of Computer Experiments (DACE) toolkit for MATLAB.[33] The initial guesses of all hyperparameters in the Gaussian process surrogates are 0.1 with a lower and upper bound of 0.001 and 300. The hyperparameters are updated for each iteration. The optimization process is outlined in Figure 3. First, the Latin hypercube sampling (LHS) method is used to generate initial samples spanning the design space. For each iteration, the algorithm advances by finding the next best parameters by maximizing the acquisition function. The evaluations of the acquisition function are based on the surrogates and do not require expensive simulations. Once the next set of parameters are determined, the MD simulations are executed to

calculate the objectives. The surrogates are updated with the results from the new sample. This algorithm repeats until a specified number of Pareto solutions are obtained.

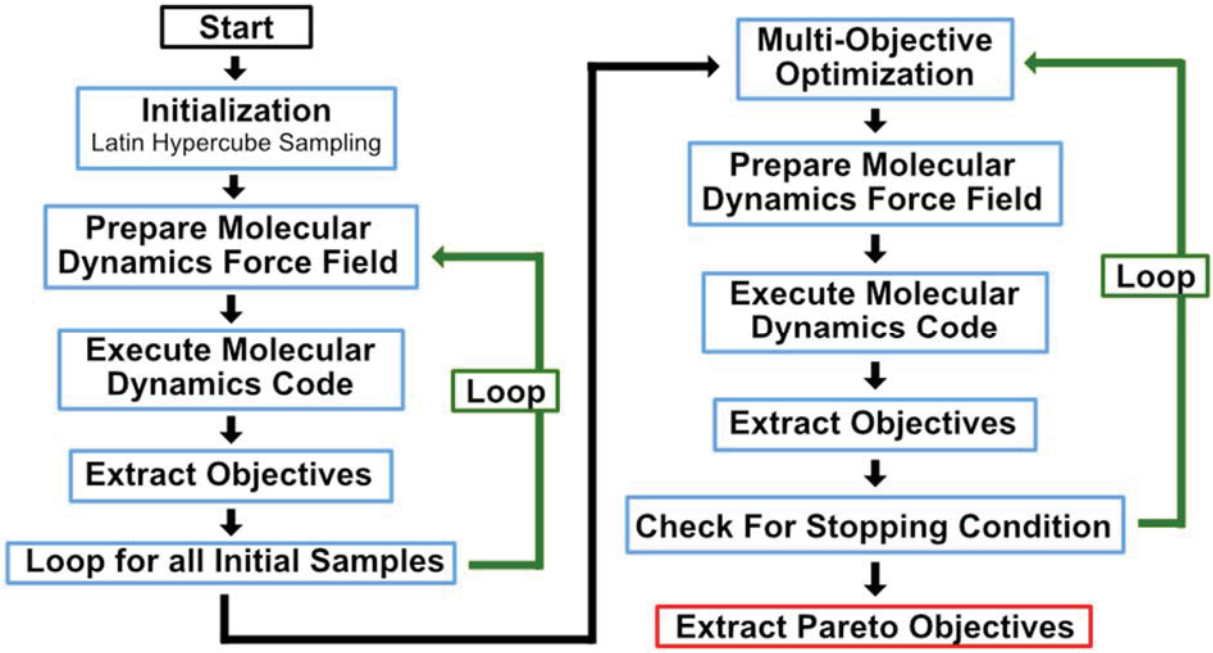

Figure 3. Flowchart detailing the optimization algorithm used to calculate the Pareto front for the molecular dynamics force field.

Results and Discussion

Coarse-Grained Force Field Model Parameterization

The MARTINI force field has been used to simulate PCL and has been parameterized mimicking the full atomistic OPLS all atom force field.[34] It has been analyzed to verify radius of gyration, end-to-end distance, temperature, and solvent transferability.[34] However, this force field is not parameterized to simulate the diffusion process for PCL. For MARTINI force fields, first hydrogens are removed and four heavy atoms need to be combined into one MARTINI particle.[19] The reduction of particles to the PCL monomer is shown in Figure 4a and Figure 4c. The four carbon atoms on the left are combined and modeled with a hydrophobic particle (C1). The next two carbon atoms and the two oxygen atoms on the right are combined and modeled by a site of intermediate hydrophilicity (Na). This coarse graining is similar to the force field developed by Raman et al.[34] Therefore, each PCL monomer can be represented as 2 particles instead of 18. Compared to the full atom model shown in Figure 4a and the united atom model shown in Figure 4b, the MARTINI force field has much fewer particles. The interaction between the C1 and Na particles is parameterized with three parameters, as shown in Figure 4d. They are the bond length and two bond angles. To simulate water in MARTINI coarse graining, four water molecules are combined into one P4 particle. The time scale for coarse grained simulations can also be modified. The time step for the simulations can be increased from 1 femtosecond utilized in full atomistic MD up to 40 femtoseconds.

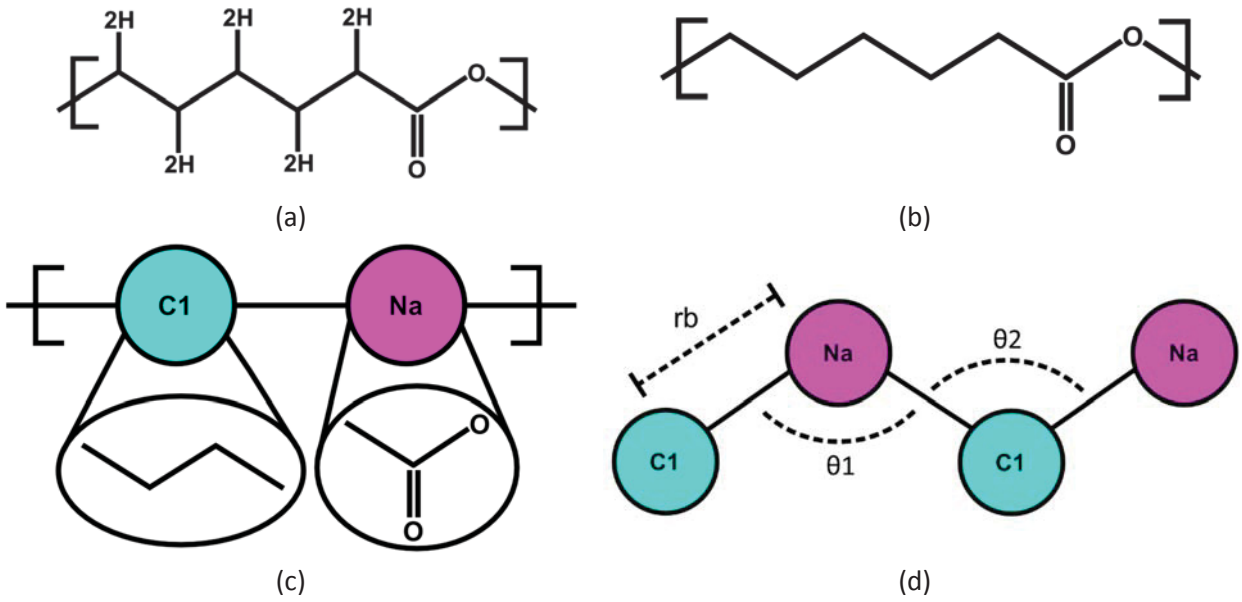

Figure 4. MARTINI coarse-grained force field for PCL monomer in comparison with (a) full atomistic model and (b) united atom model. (c) MARTINI coarse graining procedure for the individual monomers and (d) parameters required for bond and angle interactions.

The three energy terms for the MARTINI force field are U_{bond}, U_{angle}, and U_{pair} as defined below.

$$U_{bond}(r) = K_b(r - r_b)^2 \tag{1}$$

is the energy between two bonded particles, where r is the distance between the particles, r_b is the bond length corresponding to the minimum energy, and K_b is the force constant.

$$U_{angle}(\theta) = K_\theta\{cos(\theta) - cos(\theta_0)\} \tag{2}$$

is the energy of three particles associate with the angle θ between the two bonds, where θ_0 is the angle corresponding to the minimum energy, and K_θ is the force constant.

$$U_{pair}(r) = 4\epsilon\left[\left(\frac{\sigma}{r}\right)^{12} - \left(\frac{\sigma}{r}\right)^{6}\right] + S(r) \qquad (r < r_c) \tag{3}$$

is the energy between two particles that is not captured by U_{bond} or U_{angle}, where ϵ and σ are energy and distance constants respectively and are specified for each pair of MARTINI particle types[19], r_c is the cutoff distance, $S(r)$ is the smoothing function that ramps the energy and force smoothly to zero past the cutoff distance.

The force constants and minimum energy distances and angles can be specified to be more suited for specific polymers. For the Na-C1 monomer configuration, there are two angles that exist in the PCL structure. The C1-Na-C1 angle results in $K_{\theta 1}$ and θ_1, and the Na-C1-Na angle results in $K_{\theta 2}$ and θ_2 for each angle energy equation. When constant non-bonded parameters are assumed, the total energy of the system

$$U_{total} = \sum_i U_i = f(K_b, r_b, K_{\theta 1}, \theta_1, K_{\theta 2}, \theta_2) \tag{4}$$

can be calculated as a function of the variables for the bonded interactions between C1-Na and the two angles.

When generating the force field for PCL, the input variables $(K_b, r_b, K_{\theta 1}, \theta_1, K_{\theta 2}, \theta_2)$ need to be optimized to predict specific characteristics of the polymer accurately. Since the ultimate goal is to simulate the degradation of the biodegradable polymer, the modulus of elasticity (E) and the Fickian diffusion coefficient of water in the polymer matrix (D) are examined.

Molecular Dynamics Property Prediction

To perform the MD simulations, Large-scale Atomic/Molecular Massively Parallel Simulator (LAMMPS), developed at Sandia National Laboratory, is used.[35] The non-bonded interactions are defined per the MARTINI force field[19] with bonded interactions defined per the algorithm. Berendsen thermostats and barostats are used for all simulations, with 1 ps and 4 ps damping parameters, respectively. All barostats and thermostats are run at 0 atm and 300 K. To calculate the two properties of interest, two simulations are utilized. The first simulation determines the modulus of elasticity, while the second simulation calculates the diffusion coefficient of water in the polymeric matrix.

For the first simulation, the geometry is first initialized with 9 chains of 701 monomers each resulting in 80 kDa chains. Initially, a soft force field with a 0 angstrom cutoff for the non-bonded interactions is used to allow the chains to cross, coupled with a constant volume (NVT) simulation. This will ensure a realistic, entangled polymer matrix and reduce the overall equilibration time. The system is deformed to a cube of the experimental density of PCL and allowed to equilibrate for 200,000 time steps with a time step of 20 fs, while the non-bonded force field cutoff is slowly increased. The soft force field is replaced by the MARTINI force and constant pressure and enthalpy (NPH) and Langevin thermostats are then used, with incremental time steps up to 20 fs. The simulation reduces the energy of the system. Following the equilibration procedure similar to Fan et al. and Awasthi et al.,[36,37] the entire cube is then equilibrated using a constant pressure (NPT) simulation for 40 ns to ensure the total energy stabilization. It has been observed that the total energy tends to stabilize such that the absolute value of the slope of the total energy with respect to time for a 10 ns sample is less than 1 Kcal per mole per ns. This occurs after approximately 20 ns of equilibration. From here, a tensile test is performed at a 1 fs time step to extract the modulus of elasticity. Keeping two of the three dimensions at a constant pressure, the constant temperature system is deformed along the third dimension at a strain rate of 0.1 ns^{-1} until a strain of 0.05 is reached. The modulus of elasticity (E) is extracted from the data by

$$\sigma = E\epsilon + C \tag{5}$$

where σ is the stress, ϵ is the strain, and C is a constant. An example of the test results is shown in Figure 5a.

For the second simulation, the geometry is first initialized with 9 chains of 701 monomers each as well as water particles. To determine the number of P4 water particles to include in the simulation, water vapor absorption from existing experimental results were examined, which gives a range of 80 to 252 molecules depending on external water pressure.[38] From the study of Harrison et al.,[39] the number of liquid water molecules is approximately 121. For the diffusion simulation using 9 chains, 31 P4 particles are used resulting in 124 water molecules. The rest of the initialization is the same as the one in the first simulation. However, instead of a tensile test, a diffusion test is performed. To calculate the Fickian

diffusion coefficient of water through the polymer matrix, the Green Kubo relation is used, which states that the diffusion coefficient is proportional to the slope of the mean squared displacement (MSD), as

$$D = \frac{1}{2n}\langle \Delta^2 r(t) \rangle \tag{6}$$

where D is the diffusion coefficient, n is the number of dimensions, and $\langle \Delta^2 r(t) \rangle$ represents the MSD.[40] The simulation with a time step of 1 fs undergoes a constant energy and volume (NVE) simulation for 0.5 ns. The MSD is then calculated for the water molecules, and then the diffusion coefficient is determined based on eq (*6*). An example of the MSD evolutions is shown in Figure 5b.

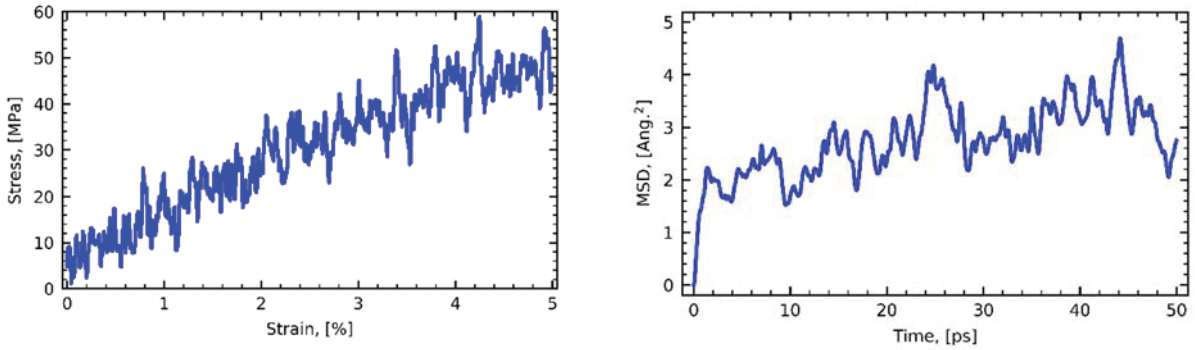

(a) (b)

Figure 5. (a) Tensile test and (b) diffusion test results for the force field parameters as defined by Raman et al.[34]

Multi-objective Bayesian Optimization

For calibration, the modulus of elasticity E and Fickian diffusion coefficient D are used to optimize the force field parameters $(K_b, r_b, K_{\theta 1}, \theta_1, K_{\theta 2}, \theta_2)$. This is done by minimizing the relative errors of the calculated E and D terms with respect to the experimental results. The objective functions are

$$f_1 = \left|(E(K_b, r_b, K_{\theta 1}, \theta_1, K_{\theta 2}, \theta_2) - E_0) \times \left(\frac{100}{E_0}\right)\right| \tag{7}$$

$$f_2 = \left|(D(K_b, r_b, K_{\theta 1}, \theta_1, K_{\theta 2}, \theta_2) - D_0) \times \left(\frac{100}{D_0}\right)\right| \tag{8}$$

where E_0 and D_0 are experimental values for the properties of PCL. These two objective functions will then be minimized simultaneously in the multi-objective optimization algorithm. The modulus of elasticity for pure PCL with a molecular weight of 80 kDa has been found to be around 429.1 MPa[41] and similar results for a 84.5 kDa sample has been found to be around 440 MPa.[42] For the purposes of optimization, a E_0 of 429.1 MPa for 80 kDa is selected. The Fickian diffusion coefficient of water in PCL is calculated to be 2.00 x 10^{-7} cm^2 per sec for a 23.2 kDa sample of PCL.[38] This was investigated with an 80 kDA sample and found to have diffusion coefficients for sorption and desorption of 4.93 x 10^{-7} and 5.60 x 10^{-7} cm^2 per sec, respectively.[43] These values have been averaged for a D_0 of 5.265 x 10^{-7} cm^2 per sec.

Our optimization problem is designed with six design variables and two objectives. To determine the ranges of design variables $K_b, r_b, K_{\theta 1}, K_{\theta 2}, \theta_1$, and θ_2, the force field parameters calculated by Raman et al.[34] are taken as the reference values, where K_b is 5.975 kcal/mol-Å^2 and the values for $K_{\theta 1}$and $K_{\theta 2}$ are 4.780 kcal/mol. Here, the range for K_b is set to be 3 to 7 kcal/mol- Å^2, and the ranges of $K_{\theta 1}$and $K_{\theta 2}$ are 2 to 7 kcal/mol, which encompass the reference values and do not over constrain the simulation. To

select the range for r_b, the maximum is based on the maximum bond length for the coarse-grained molecule, 4.18 Å. A minimum value of 3.5 Å is selected to encompass the Raman et al. value of 4.15 Å.[34] The values of θ_1 and θ_2 are constrained within a range of 90° to 180°. The LHS method is used to generate 30 initial samples spanning the design space as outlined in Table 1. Each MD simulation was run on 8 processors in parallel. After the initial 30 simulations of tensile and diffusion tests, the sequential sampling drives the simulations for a total of 10 days.

Table 1. Minimum and maximum values used for the design space of the parameters for the multi-objective optimization algorithm.

Design Variable	Minimum Value	Maximum Value
$K_b, [kcal/mol/\text{Å}^2]$	3	7
$r_b, [\text{Å}]$	3.5	4.18
$K_{\theta 1}, [kcal/mol]$	2	7
$\theta_1, [°]$	90	180
$K_{\theta 2}, [kcal/mol]$	2	7
$\theta_2, [°]$	90	180

Selection and Classification of Final Force Fields

In this example, after 338 samples, or MD simulation runs, 11 Pareto solutions are identified as shown in Figure 6. From the 11 candidate force fields on the Pareto front, a final selection needs to be made. The Pareto solutions can be examined first and narrowed down by using the maximum allowable error. Solutions that cause too much deviation from the experimental observations on any of the properties need not be considered further. One advantage of the multi-objective approach is that alternative solutions are available and users can select based on their own criterion. For instance, if the accuracy of the mean value predictions is important, a force field that results in balanced predictions of different properties can be selected. Alternatively, if the robustness of predictions is preferred, a model with the minimum variances can be selected. The selection process is demonstrated as follows.

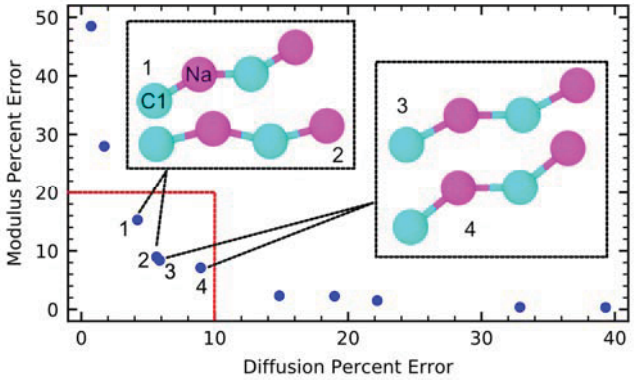

Figure 6. 11 Pareto solutions are obtained from a total of 338 simulation runs. The red lines outline the allowable error ranges, where four Pareto solutions (1 to 4) are selected for further analysis. The corresponding two units of monomers are also shown at their minimum energy states.

As shown in Figure 6, the 11 Pareto solutions do not dominate each other. Reducing the error for diffusion coefficient prediction increases the error of elastic modulus prediction. The maximum allowable error for diffusion is selected to be 10% while the maximum allowable error for the Modulus of Elasticity is selected to be 20%. These percentages are selected so that more weight is put on the diffusion process, since our ultimate goal is to predict the biodegradation of PCL. Four Pareto solutions fulfill these conditions, which are labeled 1 to 4 in Figure 6. The values of force field parameters for these four Pareto solutions are given in Table 2.

Table 2. Force field parameters for the four selected Pareto solutions for further analysis.

Property	Pareto 1	Pareto 2	Pareto 3	Pareto 4
$K_b, [Kcal/mole/Å^2]$	3.0027	3.0001	3.0001	6.9972
$r_b, [Å]$	3.5034	3.9594	4.1798	4.1799
$K_{\theta 1}, [Kcal/mole]$	2.9797	3.4553	4.8098	2.8628
$\theta_1, [degree]$	180	154.61	179.71	179.99
$K_{\theta 2}, [Kcal/mole]$	2.0076	4.037	2.0001	4.9926
$\theta_2, [degree]$	119.75	151	124.35	102.22

To further characterize each Pareto solution, we compare the simulation predictions from the four Pareto solutions with additional experimental data for the temperature dependency of the diffusion coefficient. The diffusion of the water particles through the polymer matrix is expected to follow the Stokes-Einstein such that

$$D = \frac{k_B T}{6 \pi \eta r} \tag{9}$$

where k_B is the Boltzmann constant, η is the viscosity, r is the radius of the equivalent spherical particle, and T is the temperature.[44] This implies that the diffusion of the water particles will be linearly related to the temperature of the system such that

$$D = A_1 T \tag{10}$$

where A_1 is a constant. The experimental results from Yoon et. al[38] showed that $A_1$is within a range between 0.02×10^{-7} and $0.40 \times 10^{-7}\ cm^2/\ K\ s$. The additional diffusion simulations are performed for a period of 40 ns within a temperature range of 300 K to 340 K and displayed in Figure 7a. The slope of the linear fitting is extracted from each of the four force fields. The results are listed in Table 3. The slopes of Pareto solutions 1, 2, and 3 fall within the experimental bounds, while Pareto solution 4 is above the maximum range of the experimental results. Therefore, Pareto solution 4 is unable to capture the temperature dependency of the diffusivity of water accurately.

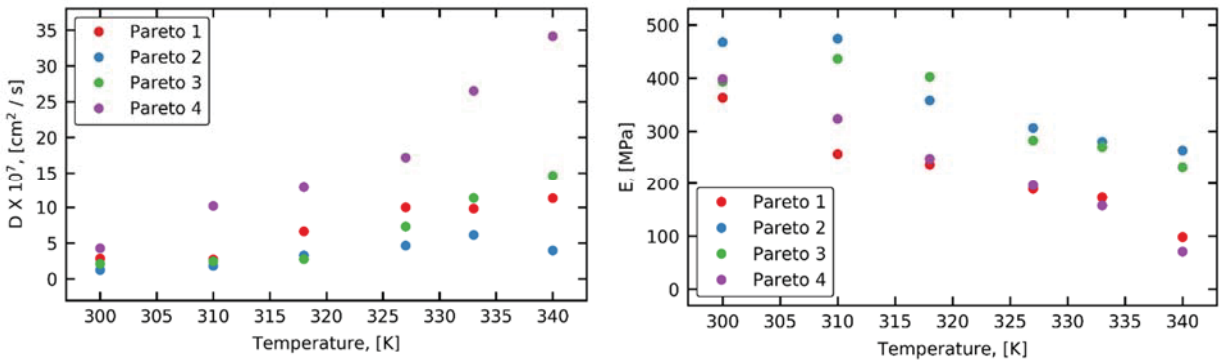

(a) (b)

Figure 7. The (a) diffusion coefficient and the (b) modulus of elasticity of the four Pareto simulations for different values of temperature ranging from 300 K to 340 K.

The time dependency of the modulus of elasticity is also applied for validation with additional experimental data. It is known that[45]

$$E = E_a \left[1 - a\frac{T}{T_m}\right] \tag{11}$$

where E_a is the modulus of elasticity at absolute zero temperature, T_m is the melting temperature, and a is a constant. This implies that the modulus of elasticity also follows a linear relationship with temperature such that

$$E = -A_2 T + E_a \tag{12}$$

where A_2 is a constant.[46–48] Experimental results showed that the range of A_2 is from 6.0 to 7.5 $MPa\ /\ K$.[49,50] Additional simulations are also performed for the modulus of elasticity with different temperatures. The results are shown in Figure 7b. Linear regression is applied and the slope is extracted for each of the four Pareto solutions. The results are also shown in Table 3. Pareto solutions 1, 2, and 4 do not fall within the experimental range of A_2. However, Pareto solutions 1 and 2 are within 2% error of the lower bound of the experimental results and Pareto solution 4 is within 5% error of the upper bound of the experimental results. Conversely, Pareto solution 3 falls far outside the range. Therefore, Pareto solution 3 is unable to capture the temperature dependency of the modulus of elasticity accurately.

Table 3. Slope constants of property values versus temperature for diffusivity and modulus of elasticity for the four Pareto solutions.[38,49,50]

Property	Experimental	Pareto 1	Pareto 2	Pareto 3	Pareto 4	Raman et al.
$A_1 \times 10^7\ [cm^2/K\ s]$	0.02 to 0.40	0.2414	0.1026	0.3280	0.7150	0.0997
$A_2, [MPa\ /\ K]$	6.0 to 7.5	5.8833	5.9356	5.0060	7.8524	2.2124

To compare the newly generated force fields with others, the temperature dependent parameters, the modulus of elasticity, and the diffusivity were also predicted with MD simulations based on the PCL force field generated by Raman et al.[34] This MARTINI force field was parameterized according to the energy characterization of OPLS. The results are also listed in Table 3. The predicted A_1 coefficient

$0.0997 \times 10^{-7}\ cm^2/\ K\ s$ is within the experimental bounds, whereas the A_2 coefficient $2.2124\ MPa\ /\ K$ falls outside the experimental bounds. The force field by Raman et al. is able to predict the temperature dependency of the diffusion coefficient, but not the modulus of elasticity. In contrast, Pareto solutions 1 and 2 are able to predict the temperature dependency for both the diffusion coefficient and the modulus of elasticity.

Additional 13 simulations for each of the four Pareto solutions are performed to calculate the diffusion coefficient and modulus of elasticity. These results are then displayed as histograms in Figure 8. The resulting mean coefficients as well as the sample standard deviation are calculated and tabulated in Table 4. The modulus of elasticity predicted from the forced field by Raman et al. was 660.0 MPa. Compared to the experimental result of 429.1 MPa,[41] there is a 54% error. In contrast, the average values predicated with the Pareto solutions 1, 2, 3, and 4 have errors of 16%, 5%, 6%, and 10%, respectively. The Fickian diffusion coefficient of water in PCL predicted from the force field by Raman et al.[34] is 0.75 x 10^{-7} cm^2/s. In comparison with the experimental result of 5.265 x 10^{-7} cm^2, the error is 86%. The mean values of diffusion coefficient predicted with the four Pareto solutions have errors of 59%, 80%, 72%, and 15% respectively. It is seen that the force field developed by Raman et al.[34] has a less accurate prediction of diffusion than that of mechanical property. In contrast, Pareto solution 4 has well-balanced predictions of both properties, which is the best choice if both properties are important. Therefore, providing users multiple options of Pareto solutions allow them to choose based on different needs of property predictions.

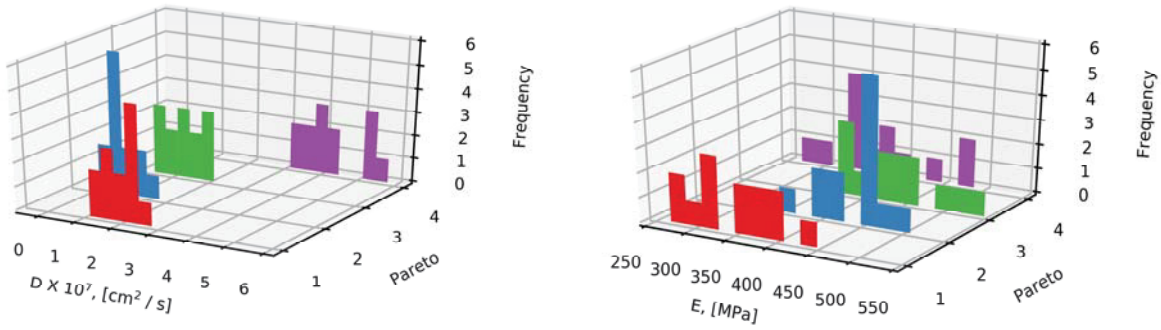

(a) (b)

Figure 8. Plots showing the histogram of the data for Pareto 1, 2, 3, and 4 for the (a) diffusion results (b) and the modulus of elasticity results.

Table 4. Mean and standard deviation for diffusivity and modulus of elasticity for 13 simulations at 300K for Pareto solutions 1 and 2.[41,43]

Property	Experimental	Pareto 1	Pareto 2	Pareto 3	Pareto 4	Raman et al.
$D \times 10^7, [cm^2/s]$	5.265	2.1692	1.0463	1.4635	4.4960	0.7536
$\sigma_D \times 10^7, [cm^2/s]$	-	0.4123	0.3624	0.4730	0.8152	0.2240
$E, [MPa]$	429.1	358.3151	449.0832	455.1388	382.9861	660.0027
$\sigma_E, [MPa]$	-	49.7011	34.9532	51.0702	61.3500	69.4932

When the robustness of the property calculations is preferred, the variances associated with the predictions need to be considered. Statistical tests can be performed to quantitatively compare variances. In this example, Pareto solutions 1 and 2 have the lowest variance in both property predictions. An F-test can be done to determine if the variances for either property calculation differ between the two. If so, the minimum variance solution can be chosen to ensure the precision when performing the diffusion simulation or modulus of elasticity calculation. The null hypothesis (H_0) is set as $\sigma_2^2 = \sigma_1^2$ for both tests. The alternative hypothesis (H_1) is set as $\sigma_{D,2}^2 < \sigma_{D,1}^2$ for the diffusion test and H_1 as $\sigma_{E,2}^2 < \sigma_{E,1}^2$ for the modulus of elasticity test. The hypotheses results in p-values of 0.3309 and 0.1185 respectively. That is, there is a 67% confidence that the variance for the diffusion coefficient estimation from the force field of Pareto solution 2 is less than that of Pareto solution 1. In addition, there is an 88% confidence that the variance for the estimated modulus of elasticity from the force field of Pareto solution 2 is less than that of Pareto Solution 1. Therefore, if precision is the most desired attribute of the force field, Pareto solution 2 could be the optimal choice, especially for the cases of extrapolation when the simulation is to predict properties under conditions that are different from those in the available experimental data.

T-tests can be performed to more quantitatively examine the accuracy of the predicted modulus of elasticity in comparison to the experimental result E_0. For these tests, the null hypothesis is H_0, is $E = E_0$ and the alternative hypothesis is H_1, is $E \neq E_0$. The resulting p-values for Pareto solutions 1, 2, 3, and 4 are 0.00025, 0.06162, 0.09088, and 0.01895 respectively. This implies that Pareto solution 3 has the highest confidence that the force field can accurately predict the modulus of elastic. Therefore, if the modulus of elasticity calculation is of the only concern, Pareto solution 3 is recommended. However, if there is a desire to have a balance between accuracy and precision for the modulus of elasticity, Pareto solution 2 is recommended instead.

Similarly T-tests can be performed to quantitatively examine the accuracy of the predicted diffusion coefficient. For these tests, the null hypothesis is H_0, is $D = D_0$ and the alternative hypothesis is H_1, is $D \neq D_0$. The resulting p-values for Pareto solutions 1, 2, 3, and 4 are 10^{-12}, 10^{-14}, 10^{-12}, and 0.0053 respectively. This implies that the force fields of Pareto solutions 1, 2, and 3 are unlikely to accurately calculate the diffusion coefficient and will have to be calibrated further with the appropriate time step if used. There is a higher confidence that the force field of Pareto solution 4 can accurately predict the diffusion coefficient without requiring further time step calibration for a 1 fs time step. If a different time step is used, the diffusion coefficient calculation should be calibrated as with the MARTINI force field, given that different time steps will affect the time-dependent diffusion coefficient calculation.[19] Therefore, if the diffusion coefficient calculation at 1 fs without performing a calibration is most important, then Pareto solution 4 is recommended.

The above discussions show that tradeoffs between the choices of Pareto solutions are needed in different scenarios and applications. The final choice should be selected based on the application-specific criteria for accuracy and robustness of property predictions. It has been demonstrated that considering additional attributes such as the temperature dependency of properties can be useful in making choices. Statistical tests can help in the decision making process.

To further examine the effectiveness of the multi-objective Bayesian optimization algorithm in sequential sampling, a traditional random sampling approach is also taken to sample 338 force fields from the same design space based on the LHS method. The diffusion coefficient and modulus of elasticity are

similarly predicted by running the simulations. The simulation runs which result in relative errors that are less than 50% for the two predicted properties from the Bayesian optimization and the LHS method are plotted in Figure 9. The Bayesian optimization algorithm obtains 81 samples that have less than 50% error compared to 33 samples the LHS method, which means that our new approach leads to a higher probability of obtaining samples that minimize both objectives.

Convergence and diversity are two common criteria to measure the quality of Pareto fronts. Convergence measures how close a Pareto front converges to the true optima of both objectives and minimizes the infeasible region, as illustrated in Figure 2. Diversity measures how representative the Pareto front is for all possible optima in the wide spread of objective values. Here the modified hyperarea difference (MHD) and modified overall spread (MOS) quality metrics[17] are used to quantitatively measure convergence and diversity respectively. The MHD is defined as

$$MHD = \sum_{i=1}^{n-1}\big((x_{i+1} - x_i)(y_i - y_n)\big) \tag{13}$$

for n sorted Pareto solutions with objective values (x_i, y_i)'s where $x_i < x_{i+1}$, $y_i > y_{i+1}$ $(\forall i = 1, \dots, n-1)$. That is, the MHD measures the area beneath the Pareto front. The MOS is defined as

$$MOS = (x_n - x_1)(y_1 - y_n) \tag{14}$$

with sorted values (x_i, y_i)'s. Smaller MHD and larger MOS are better. The MHD and MOS values of the Pareto front out of the 338 samples obtained by the Bayesian optimization algorithm are 0.023 and 0.186, respectively. The MHD and MOS values of the Pareto front obtained by the LHS method are 0.0422 and 0.945, respectively. The Bayesian optimization method is able to identify the Pareto solutions more exhaustively in the desirable region with small prediction errors for both properties, instead of spending simulation time in the region where large errors for either property occur.

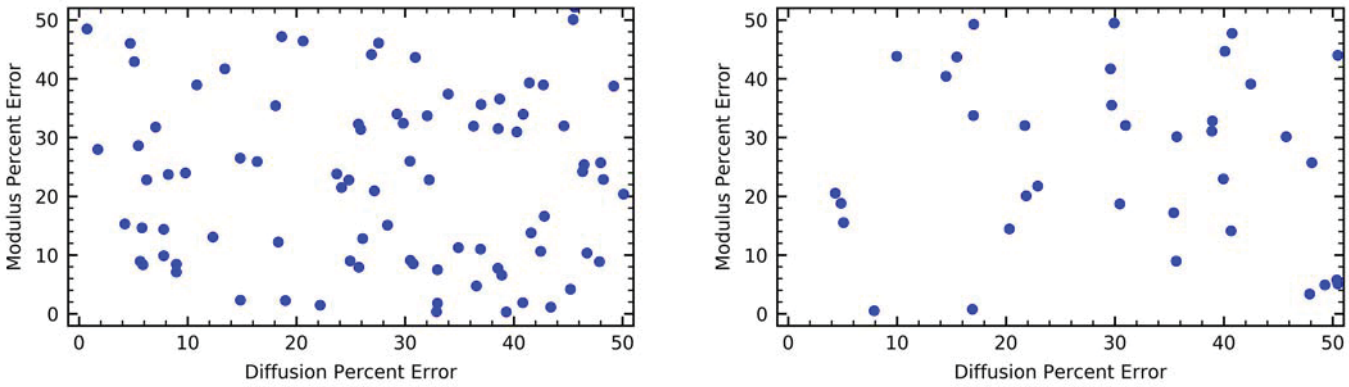

Figure 9. Samples that have less than 50% error for both objectives for the (a) Bayesian optimization and (b) Latin hypercube sampling methods.

Conclusions

This paper outlines a new methodology using multi-objective optimization to calibrate force fields based on multiple properties of interest. The methodology includes an efficient sequential sampling through multi-objective Bayesian optimization to identify Pareto solutions, and statistical analyses for force field selection with the criteria of accuracy and robustness. The Pareto solutions provide

users the options to choose based on the application-specific criteria and preferences. The method has been applied to generate new MARTINI force fields for PCL. The developed force field is capable of predicting both the modulus of elasticity and diffusion coefficient of water through PCL accurately.

The proposed multi-objective Bayesian optimization method for force field calibration has been demonstrated with six design variables and two objectives. The ability to extend it to higher dimensionality and allow for an increase in design variables and objectives is needed. Increasing the number of design variables leads to an exponential growth of the number of samples required to establish reliable Gaussian process surrogate models,[51] which is not desirable when simulations are expensive.

Not only the number of design variables affects the efficiency of Bayesian optimization, the number of samples to construct the Pareto front also increases as the number of objectives increases.[14] For instance, the 2D Pareto front in this study was constructed with 338 simulations. Increasing to three objectives requires us to construct a 3D surface as the Pareto front. The number of samples will also grow exponentially with more objectives are considered, even though the proposed multi-objective Bayesian optimization approach is able to better handle higher dimensionality in objectives than other multi-objective optimization. One way to remedy this curse of dimensionality would be to examine the possibility of parallelizing MD simulations and sampling. This would increase the required computational resources but decrease the overall time. A caveat to this would be new acquisition functions that allow for sequential batch sampling for parallelization.

In this paper, only a coarse-grained molecular dynamics for polymers is examined. Though coarse graining is useful for our particular application, full-atom MD models for polymers are still necessary for capturing the electrostatic effects for many applications. For full-atom MD models of PCL, there can be a total of five types of atoms in the monomer: a backbone carbon, a carboxyl group carbon, two carboxyl group oxygens, and a backbone hydrogen. With no restrictions, this will result in 120 non-bonded interactions and 4 independent charges for a total of 244 design variables for interatomic potentials. Simplification needs to be made to use more generic force field parameterization as a starting point and only specific interactions in the overall property are utilized for PCL. Simplification can also be done on the electrostatic forces and only four independent charges are included in the design variables. Therefore, when the full-atom simulation is applied for polymers and proteins, the number of parameters to be calibrated can exhibit quadratic growth. This will increase the number of samples necessary to form the Pareto front, and thus the time to run the calibration process. Prior knowledge of force field interactions may reduce the overall number of design variables, making the development of full-atom polymer and protein force fields more efficient.

The force fields for metal-based applications, such as EAM, rely on non-bonded interactions between all of the atom types defined in the force field as well as electron cloud density. For an EAM force field that captures m number of atom types, there will be $m(m+1)/2$ non-bonded interactions, m embedding functions, and m electron cloud contribution functions, which lead to a total of $m(m+1)/2+2m$ functions. Since each interaction and function requires two design parameters, each force field requires approximately $m(m+1)+4m$ design parameters, which may be reduced based on prior knowledge. An example of reduction is adding in a third atom type into an existing EAM potential that is parameterized for two atom types. This would require an additional 3 non-bonded interactions, 1

embedding function, and 1 electron cloud contribution function, resulting in a total of 10 design parameters in the optimization process.

This method has been shown to work efficiently with two properties as the objectives in the optimization. Adding more objectives will increase the number of simulations that are necessary to form a credible Pareto solution set. Future work will need to further improve the efficiency of sampling for force fields with more parameters and more properties.

Author Information

Corresponding Author

*E-mail: yan.wang@me.gatech.edu. Phone: +1 404 8944714. Fax: +1 404 8949342

Author Contributions

JS, TH, and YW conceived the methodology. JS wrote the code, performed the simulations, and conducted the data analysis in collaboration with TH and YW. MT helped conduct diffusion MD simulations. LS helped write code for the multi-objective optimization. JS, TH, and YW wrote the manuscript.

Notes

The authors declare no competing financial interest.

Acknowledgments

This research was supported in part by the National Science Foundation through grants IGERT-1258425 and CMMI-1663227, as well as the research cyberinfrastructure resources and services provided by the Partnership for an Advanced Computing Environment (PACE) at the Georgia Institute of Technology.

References

(1) Foiles, S. M.; Hoyt, J. J. Computation of Grain Boundary Stiffness and Mobility from Boundary Fluctuations. *Acta Mater.* **2006**, *54* (12), 3351–3357.

(2) Ko, W.-S.; Grabowski, B.; Neugebauer, J. Development and Application of a Ni-Ti Interatomic Potential with High Predictive Accuracy of the Martensitic Phase Transition. *Phys. Rev. B* **2015**, *92* (13), 134107.

(3) Mayo, S. L.; Olafson, B. D.; Goddard, W. A. DREIDING: A Generic Force Field for Molecular Simulations. *J. Phys. Chem.* **1990**, *94* (26), 8897–8909.

(4) Kaminski, G. A.; Friesner, R. A.; Tirado-Rives, J.; Jorgensen, W. L. Evaluation and Reparametrization of the OPLS-AA Force Field for Proteins via Comparison with Accurate Quantum Chemical Calculations on Peptides. *J. Phys. Chem. B* **2001**, *105* (28), 6474–6487.

(5) Jorgensen, W. L.; Maxwell, D. S.; Tirado-Rives, J. Development and Testing of the OPLS All-Atom Force Field on Conformational Energetics and Properties of Organic Liquids. *J. Am. Chem. Soc.* **1996**, *118* (45), 11225–11236.

(6) Scott, W. R. P.; Hünenberger, P. H.; Tironi, I. G.; Mark, A. E.; Billeter, S. R.; Fennen, J.; Torda, A. E.; Huber, T.; Krüger, P.; Van Gunsteren, W. F. The GROMOS Biomolecular Simulation Program Package. *J. Phys. Chem. A* **1999**, *103* (19), 3596–3607.

(7) Gime, X.; Bofill, J. M.; Gonza, J. Algorithm to Evaluate Rate Constants for Polyatomic Chemical Reactions. II. Applications. *J. Comput. Chem.* **2007**, *28*, 2111–2121.

(8) Case, D. A.; Cheatham, T. E.; Darden, T.; Gohlke, H.; Luo, R.; Merz, K. M.; Onufriev, A.; Simmerling, C.; Wang, B.; Woods, R. J. The Amber Biomolecular Simulation Programs. *J. Comput. Chem.* **2005**, *26* (16), 1668–1688.

(9) Martinez, J.; Liang, T.; Sinnott, S. B.; Phillpot, S. R. A Third-Generation Charge Optimized Many Body (COMB3) Potential for Nitrogen-Containing Organic Molecules. *Comput. Mater. Sci.* **2017**, *139*, 153–161.

(10) Phillpot, S. R.; Antony, A. C.; Shi, L.; Fullarton, M. L.; Liang, T.; Sinnott, S. B.; Zhang, Y.; Biner, S. B. Charge Optimized Many Body (COMB) Potentials for Simulation of Nuclear Fuel and Clad. *Comput. Mater. Sci.* **2018**, *148*, 231–241.

(11) Sun, H. Ab Initio Calculations and Force Field Development for Computer Simulation of Polysilanes. *Macromolecules* **1995**, *28* (3), 701–712.

(12) Martinez, J. A.; Chernatynskiy, A.; Yilmaz, D. E.; Liang, T.; Sinnott, S. B.; Phillpot, S. R. Potential Optimization Software for Materials (POSMat). *Comput. Phys. Commun.* **2016**, *203*, 201–211.

(13) Ragasa, E. J.; O'Brien, C. J.; Henning, R. G.; Foiles, S. M.; Phillpot, S. R. Multi-Objective Optimization of Interatomic Potentials with Application to MgO. *Model. Simul. Mater. Sci. Eng.* **2019**, 1–23.

(14) Mcdonagh, J. L.; Shkurti, A.; Bray, D. J.; Anderson, R. L.; Pyzer-Knapp, E. O. Utilizing Machine Learning for Efficient Parameterization of Coarse Grained Molecular Force Fields. *J. Chem. Inf. Model.* **2019**.

(15) Dequidt, A.; Solano Canchaya, J. G. Bayesian Parametrization of Coarse-Grain Dissipative Dynamics

Models. *J. Chem. Phys.* **2015**, *143* (8).

(16) Liu, P.; Shi, Q.; Dauḿ, H.; Voth, G. A. A Bayesian Statistics Approach to Multiscale Coarse Graining. *J. Chem. Phys.* **2008**, *129* (21).

(17) Shu, L.; Jiang, P.; Shao, X.; Wang, Y. A New Multi-Objective Bayesian Optimization Formulation With the Acquisition Function for Convergence and Diversity. *J. Mech. Des.* **2020**, *142* (9), 1–23.

(18) Zhan, D.; Cheng, Y.; Liu, J. Expected Improvement Matrix-Based Infill Criteria for Expensive Multiobjective Optimization. *IEEE Trans. Evol. Comput.* **2017**, *21* (6), 956–975.

(19) Marrink, S. J.; Risselada, H. J.; Yefimov, S.; Tieleman, D. P.; De Vries, A. H. The MARTINI Force Field: Coarse Grained Model for Biomolecular Simulations. *J. Phys. Chem. B* **2007**, *111* (27), 7812–7824.

(20) Yesylevskyy, S. O.; Schäfer, L. V.; Sengupta, D.; Marrink, S. J. Polarizable Water Model for the Coarse-Grained MARTINI Force Field. *PLoS Comput. Biol.* **2010**, *6* (6), 1–17.

(21) De Jong, D. H.; Singh, G.; Bennett, W. F. D.; Arnarez, C.; Wassenaar, T. A.; Schäfer, L. V.; Periole, X.; Tieleman, D. P.; Marrink, S. J. Improved Parameters for the Martini Coarse-Grained Protein Force Field. *J. Chem. Theory Comput.* **2013**, *9* (1), 687–697.

(22) Monticelli, L.; Kandasamy, S.; Periole, X.; Larson, R.; Tieleman, D.; Marrink, S. The MARTINI Coarse-Grained Force Field: Extension to Proteins. *J. Chem. Theor. Comp.* **2008**, *4*, 819–834.

(23) Rossi, G.; Monticelli, L.; Puisto, S. R.; Vattulainen, I.; Ala-Nissila, T. Coarse-Graining Polymers with the MARTINI Force-Field: Polystyrene as a Benchmark Case. *Soft Matter* **2011**, *7* (2), 698–708.

(24) Salerno, K. M.; Bernstein, N. Persistence Length, End-to-End Distance, and Structure of Coarse-Grained Polymers. *J. Chem. Theory Comput.* **2018**, *14* (4), 2219–2229.

(25) Yu, Z.; Lau, D. Development of a Coarse-Grained α-Chitin Model on the Basis of MARTINI Forcefield. *J. Mol. Model.* **2015**, *21* (5).

(26) Pervaje, A. K.; Tilly, J. C.; Inglefield, D. L.; Spontak, R. J.; Khan, S. A.; Santiso, E. E. Modeling Polymer Glass Transition Properties from Empirical Monomer Data with the SAFT-γ Mie Force Field. *Macromolecules* **2018**, acs.macromol.8b01734.

(27) Ruiz-Morales, Y.; Romero-Martínez, A. Coarse-Grain Molecular Dynamics Simulations to Investigate the Bulk Viscosity and Critical Micelle Concentration of the Ionic Surfactant Sodium Dodecyl Sulfate (SDS) in Aqueous Solution. *J. Phys. Chem. B* **2018**, *122* (14), 3931–3943.

(28) Wang, H.; Wang, Z.; Lv, Q.; Li, C.; Du, Z.; Sun, S.; Hu, S. Mechanism of Foam Film Destruction Induced by Emulsified Oil: A Coarse-Grained Simulation Study. *J. Phys. Chem. C* **2018**, *122* (46), 26438–26446.

(29) Fu, P.; Yan, M.; Zeng, M.; Wang, Q. Sintering Process Simulation of a Solid Oxide Fuel Cell Anode and Its Predicted Thermophysical Properties. *Appl. Therm. Eng.* **2017**, *125*, 209–219.

(30) Perrin, E.; Schoen, M.; Coudert, F. X.; Boutin, A. Structure and Dynamics of Solvated Polymers near a Silica Surface: On the Different Roles Played by Solvent. *J. Phys. Chem. B* **2018**, *122* (16), 4573–4582.

(31) Torchi, A.; Bochicchio, D.; Pavan, G. M. How the Dynamics of a Supramolecular Polymer

Determines Its Dynamic Adaptivity and Stimuli-Responsiveness: Structure-Dynamics-Property Relationships from Coarse-Grained Simulations. *J. Phys. Chem. B* **2018**, *122* (14), 4169–4178.

(32) Močkus, J. On Bayesian Methods for Seeking the Extremum. In *Lecture Notes in Computer Science (including subseries Lecture Notes in Artificial Intelligence and Lecture Notes in Bioinformatics)*; Springer Verlag, 1975; Vol. 27 LNCS, pp 400–404.

(33) Lophaven, S.; Nielsen, H.; Søndergaard, J. *DACE - A MATLAB Kriging Toolbox Version 2.0, Technical Report IMM-TR-2002-12*; 2002.

(34) Raman, A. S.; Vishnyakov, A.; Chiew, Y. C. A Coarse-Grained Model for PCL: Conformation, Self-Assembly of MePEG-b-PCL Amphiphilic Diblock Copolymers. *Mol. Simul.* **2017**, *43* (2), 92–101.

(35) Plimpton, S. Fast Parallel Algorithms for Short – Range Molecular Dynamics. *J. Comput. Phys.* **1995**, *117* (June 1994), 1–19.

(36) Fan, C. F.; Çağin, T.; Chen, Z. M.; Smith, K. A. Molecular Modeling of Polycarbonate. 1. Force Field, Static Structure, and Mechanical Properties. *Macromolecules* **1994**, *27* (9), 2383–2391.

(37) Awasthi, A. P.; Lagoudas, D. C.; Hammerand, D. C. Modeling of Graphene-Polymer Interfacial Mechanical Behavior Using Molecular Dynamics. *Model. Simul. Mater. Sci. Eng.* **2009**, *17* (1).

(38) Yoon, J.; Jung, H.; Kim, M.; Park, E. Diffusion Coefficient and Equilibrium Solubility of Water Molecules in Biodegradable Polymers. *J. Appl. Polym. Sci.* **2000**, *77* (2), 1716–1722.

(39) Harrison, K. L.; Jenkins, M. J. The Effect of Crystallinity and Water Absorption on the Dynamic Mechanical Relaxation Behaviour of Polycaprolactone. *Polym. Int.* **2004**, *53* (9), 1298–1304.

(40) Wang, J.; Hou, T. Application of Molecular Dynamics Simulations in Molecular Property Prediction II: Diffusion Coefficient. *J. Comput. Chem.* **2011**, *32* (16), 3505–3519.

(41) Rosa, D. S.; Neto, I. C.; Calil, M. R.; Pedroso, A. G.; Fonseca, C. P.; Neves, S. Evaluation of the Thermal and Mechanical Properties of and Their Blends. *J. Appl. Polym. Sci.* **2004**, *91*, 3909–3914.

(42) K. Ragaert, L. Cardon, I. De Baere, J. D. Bulk Mechanical Porperties of Thermoplastic. *Conf. 6th Polym. Mould. Innov. Conf.* **2014**, No. January 2015.

(43) Galizia, M.; La Manna, P.; Mensitieri, G.; Pannico, M.; Musto, P. Diffusion in Polymers as Investigated by Two-Dimensional Correlation Spectroscopy: The H2O/PCL System. *J. Mol. Struct.* **2014**, *1069* (1), 290–298.

(44) Reeks, M. W. Stokes-Einstein Equation. In *A-to-Z Guide to Thermodynamics, Heat and Mass Transfer, and Fluids Engineering*; Begellhouse.

(45) Courtney, T. H. *Mechanical Behavior of Materials*; McGraw Hill, 2000.

(46) Brammer, J. A.; Percival, C. M. Elevated-Temperature Elastic Moduli of 2024 Aluminum Obtained by a Laser-Pulse Technique. *Exp. Mech.* **1970**, *10* (6), 245–250.

(47) Rojas, J. I.; Crespo, D. Modeling of the Effect of Temperature, Frequency, and Phase Transformations on the Viscoelastic Properties of AA 7075-T6 and AA 2024-T3 Aluminum Alloys. *Metall. Mater. Trans. A Phys. Metall. Mater. Sci.* **2012**, *43* (12), 4633–4646.

(48) Sutton, P. M. The Variation of the Elastic Constants of Crystalline Aluminum with Temperature

between 63°K and 773°K. *Phys. Rev.* **1953**, *91* (4), 816–821.

(49) Uto, K.; Ebara, M.; Aoyagi, T. Temperature-Responsive Poly(ε-Caprolactone) Cell Culture Platform with Dynamically Tunable Nano-Roughness and Elasticity for Control of Myoblast Morphology. *Int. J. Mol. Sci.* **2014**, *15* (1), 1511–1524.

(50) Gassner, F.; Owen, A. J. Physical Properties of Poly(β-Hydroxybutyrate)-Poly(ϵ-Caprolactone) Blends. *Polymer (Guildf).* **1994**, *35* (10), 2233–2236.

(51) Tran, A.; Tran, M.; Wang, Y. Constrained Mixed-Integer Gaussian Mixture Bayesian Optimization and Its Applications in Designing Fractal and Auxetic Metamaterials. *Struct. Multidiscip. Optim.* **2019**, *59* (6), 2131–2154.

TOC Graphic